Materials Horizons

ROYAL SOCIETY OF CHEMISTRY

COMMUNICATION

View Article Online
View Journal

Cite this: DOI: 10.1039/d5mh00667h

Received 10th April 2025,
Accepted 2nd June 2025

DOI: 10.1039/d5mh00667h

rsc.li/materials-horizons

Cross-dimensional assembly of MXene/SiO_2/KNF composite aerogels for radar and infrared stealth†

Shuo Zhang,‡[a] Fushuo Wu,‡[a] Feiyue Hu,[a] Peiying Hu,[ab] Miaoping Li,[a] Peng Zeng,[a] Peigen Zhang,*[a] Tianyu Wang,[a] Shuangshuang Chen,[a] Jian Liu,[ad] Longzhu Cai[c] and ZhengMing Sun*[a]

Radar/infrared-compatible stealth materials enhance survivability by reducing the radar cross-section and suppressing infrared signatures. However, the significant differences in frequency characteristics across electromagnetic wavebands present challenges in optimizing a cross-band electromagnetic response. To address this issue, we propose a cross-dimensional integration strategy. Zero-dimensional (0D) SiO_2 aerogel particles with low thermal conductivity act as the infrared radiation modulation component and two-dimensional (2D) $Ti_3C_2T_x$ MXene nanosheets with high electronic conductivity function as the electromagnetic wave-responsive component; the 0D and 2D functional components are directionally anchored onto one-dimensional (1D) Kevlar nanofiber (KNF) surfaces through hydrogen bonding, cooperatively constructing a monolithic interconnected network structure. The as-designed MXene/SiO_2/KNF aerogel (MSKA) has a bionic-inspired "root–soil" structure, which effectively reduces infrared radiation intensity through multiple scattering effects and enhances electromagnetic wave attenuation by optimizing spatial impedance matching and introducing multiple loss mechanisms. The MSKA exhibits excellent microwave absorption, achieving a minimum reflection loss (RL) of −64.69 dB at a thickness of 1.83 mm, with an effective absorption bandwidth (RL < −10 dB) covering 7.2 GHz; thermal testing reveals a surface temperature difference of 123.1 °C under a 175 °C heat source, indicating a significant reduction in infrared radiation intensity. This assembly strategy, enabling independent regulation of electromagnetic loss and thermal conduction through multidimensional integration, provides new insights for developing lightweight, high-performance, and multispectral stealth materials.

New concepts

This study introduces a cross-dimensional assembly design that integrates 0D–1D–2D components into a unified aerogel system to address multispectral stealth challenges. By anchoring 0D SiO_2 particles and 2D $Ti_3C_2T_x$ MXene onto 1D Kevlar nanofibers (KNFs) through hydrogen-bond-directed assembly, a biomimetic "root–soil" architecture is constructed to independently regulate electromagnetic (EM) wave absorption and infrared radiation suppression. The 2D MXene nanosheets establish a conductive network, enhancing dielectric loss *via* electron hopping and multiple polarization effects, while the 0D SiO_2 particles reduce thermal conductivity and minimize infrared emission through localized insulation effects and hierarchical pore scattering. The $Ti_3C_2T_x$-decorated 1D KNF framework extends EM wave propagation paths, amplifying attenuation while maintaining structural integrity. This cross-dimensional integration strategy enables dual functionality: broadband microwave absorption (minimum reflection loss: −64.69 dB, effective absorption bandwidth: 7.2 GHz), and infrared stealth (ΔT = 123.1 °C at 175 °C). The material's ultra-low density (5–30 mg cm^{-3}) underscores its practicality for lightweight applications.

1. Introduction

With the development of modern detection technology towards multi-spectrum collaborative detection, traditional single-spectrum stealth materials are increasingly unable to meet the concealment needs of battlefield environments. The development of composites with both radar and infrared stealth functions has become a current research hotspot.[1–4] Radar stealth materials primarily achieve low detectability by dissipating electromagnetic wave

[a] State Key Laboratory of Engineering Materials for Major Infrastructure, School of Materials Science and Engineering, Southeast University, Nanjing 211189, P. R. China. E-mail: zhpeigen@seu.edu.cn, zmsun@seu.edu.cn
[b] Swiss Federal Laboratories for Materials Science and Technology, Empa, Dübendorf 8600, Switzerland
[c] The State Key Laboratory of Millimeter Waves, School of Information Science and Engineering, Southeast University, Nanjing 210096, P. R. China
[d] Nantong Lintex Advanced Materials Co., Ltd, Nantong 226000, P. R. China

† Electronic supplementary information (ESI) available. See DOI: https://doi.org/10.1039/d5mh00667h

‡ Shuo Zhang and Fushuo Wu contributed equally to this work.

energy, converting incident electromagnetic waves into forms such as thermal energy, with the core goal of reducing target echo intensity and enhancing absorption efficiency. In contrast, infrared stealth materials use surface thermal radiation regulation strategies, employing reflection interface designs or temperature control technologies with phase-change materials to suppress the infrared radiation difference between the target and the background.[5–8] Notably, radar stealth requires materials to have impedance matching characteristics and electromagnetic loss capabilities to achieve efficient wave absorption, while infrared stealth requires materials with low emissivity surfaces to reduce radiation signatures. The fundamental contradictions in physical mechanisms and design requirements between the two pose a core challenge in the development of multi-spectrum compatible stealth technology. Therefore, how to regulate the functional differences between radar and infrared detection bands to achieve efficient multi-spectrum compatible stealth remains an urgent scientific issue in the field of stealth materials.

Existing radar stealth material systems primarily include functional materials such as nanomaterials,[9,10] doped semiconductor materials,[11] and conductive polymer materials.[6] Nanomaterials demonstrate stable electromagnetic response properties. However, their complex synthesis routes and high production costs hinder large-scale implementation. Doped semiconductor materials offer advantages in processing simplicity and mass production feasibility. Yet, their susceptibility to environmental interference demands improved stability for reliable performance. Traditional conductive polymers encounter a critical limitation due to strong π–π interactions among molecular chains. These interactions lead to intrinsic brittleness, which facilitates structural defect generation during melt-processing stages. Consequently, their practical adoption in engineering applications remains severely constrained. In this context, two-dimensional transition metal carbides ($Ti_3C_2T_x$ MXenes) have shown broad application prospects in the field of electromagnetic wave absorption due to their excellent electrical conductivity, high specific surface area, tunable electrical properties, and rich polar functional groups (such as –OH, –O, and –F).[3,12–17] Additionally, MXenes exhibit very low emissivity characteristics in the 8–14 μm mid-infrared atmospheric window[18] and demonstrates excellent infrared stealth performance over a wide temperature range.[19] This dual advantage of the electromagnetic loss and infrared regulation makes MXenes ideal candidates for radar/infrared compatible stealth materials. However, the high conductivity of MXenes causes a severe mismatch between its intrinsic impedance and free space, enhancing interface reflection and hindering its electromagnetic wave attenuation capability.[12] Furthermore, according to the Stefan–Boltzmann law, infrared stealth materials need to synergistically reduce the target temperature and emissivity to suppress the infrared radiation difference between the target and the background.[20] However, the high thermal conductivity of MXenes causes the surface temperature to rise rapidly with the target temperature, weakening its infrared stealth effect. Therefore, optimizing MXene's impedance matching and thermal insulation properties is key to overcoming the bottleneck of radar/infrared compatible stealth. SiO_2 aerogels, with their nanoscale pores and high porosity, exhibit extremely low density and thermal conductivity, effectively insulating heat conduction.[21] As porous dielectric materials, their unique dielectric properties can effectively regulate the electromagnetic parameters of composites. Thus, combining SiO_2 aerogels with MXenes can improve impedance matching through dielectric modulation and maintain infrared stealth performance in high-temperature environments by leveraging their thermal insulation properties. Currently, MXene–SiO_2 composites are mainly achieved through electrostatic self-assembly and sol–gel methods. Electrostatic self-assembly, which relies on the electrostatic attraction between charged groups, results in weak interfacial bonding and reduced mechanical properties.[22] The sol–gel method involves *in situ* generation of SiO_2 on the MXene surface to construct MXene/SiO_2 composites, but the lack of flexibility in the SiO_2 coating layer increases the risk of brittle fracture in the composites.[23–26] Therefore, developing an MXene/SiO_2 composite strategy with strong interfacial bonding and structural flexibility holds significant research value.

"Root–soil" composite systems, as a typical multi-scale three-dimensional network structure in nature, achieve soil and water conservation and slope stability through mechanical interlocking and interfacial friction between roots and soil particles. This provides significant inspiration for the multi-dimensional integrated bionic structure design of composites. By simulating the multi-level anchoring mechanism at the "root–soil" interface, artificial three-dimensional network structures can be constructed to achieve strong bonding between components of different dimensions, significantly enhancing the interfacial bonding strength between heterogeneous materials. Kevlar nanofibers (KNFs) exhibit excellent mechanical strength and thermal stability due to their unique anisotropic structure and strong interactions (such as hydrogen bonds, π–π stacking, and van der Waals forces) between poly-*p*-phenylene terephthalamide (PPTA) chains.[27] Additionally, studies have shown that the abundant oxygen-containing functional groups (such as $–NH_2$, –OH) on the surface of KNFs can form strong hydrogen bond networks with MXene[28] and SiO_2[29] to enhance interfacial bonding. This bidirectional affinity makes KNFs an ideal skeleton material for constructing biomimetic "root–soil" composite systems, theoretically enabling the simultaneous resolution of weak interfacial bonding and structural brittleness issues in MXene/SiO_2 composite systems through the stress transfer mechanism of three-dimensional networks.

This study employed a cross-dimensional integration strategy to successfully prepare an MXene/SiO_2/Kevlar nanofiber composite aerogel (MSKA) with both high-efficiency radar/infrared compatible stealth properties. Zero-dimensional (0D) SiO_2 aerogel particles, two-dimensional (2D) MXene nanosheets, and one-dimensional (1D) Kevlar nanofibers were integrated into a three-dimensional (3D) biomimetic "root–soil" structure, achieving synergistic enhancement multiple components. Under the action of a 3D hydrogen bond network, KNFs anchored discrete SiO_2 particles and MXene nanosheets into an integrated whole. This structural design effectively addressed the brittleness

problem of traditional MXene/SiO_2 composite aerogels and significantly improved the mechanical stability of the composite system through the stress transfer mechanism at the fiber–particle interface. The synergistic effect of the 3D conductive network and the low-dielectric SiO_2 particles optimized the impedance matching characteristics, enabling the composite aerogel to achieve a minimum reflection loss value (RL_{min}) of −64.69 dB at a low thickness of 1.83 mm, with an effective absorption bandwidth (EAB) covering 7.2 GHz, indicating excellent wide-band electromagnetic wave absorption capability. In terms of infrared stealth, the low thermal conductivity of the SiO_2 aerogel significantly reduced the surface temperature rise rate by inhibiting heat conduction. At an ambient temperature of 175 °C, a temperature gradient of over 120 °C could be formed between the bottom and surface of the composite aerogel, while the low infrared emissivity of MXenes further weakened the radiation intensity in the mid-to-far infrared band. The method adopted in this study achieved synergistic optimization of mechanical stability, wide-band electromagnetic absorption, and thermal protection/infrared stealth performance of the composite system, providing a new design paradigm for multifunctional stealth materials.

2. Experimental section

2.1. Materials

Ti_3AlC_2 (325 mesh, 99%) was procured from Forsman Scientific Co., Ltd (China), while lithium fluoride (LiF, 99%) and tetrabutylammonium hydroxide (TBAOH, 25% aqueous solution) were obtained from Aladdin Reagent Co., Ltd (China). Hydrochloric acid (HCl, 36–38%) and dimethyl sulfoxide (DMSO) were supplied by China National Pharmaceutical Group Co., Ltd (China). Additionally, potassium hydroxide (KOH), ethyl acetate (EA), and *tert*-butanol (TBA) were sourced from Macklin Biochemical Co., Ltd (China). Kevlar 1000D was acquired from DuPont Co., Ltd (USA).

2.2. Preparation of $Ti_3C_2T_x$ MXene nanosheets

The aluminum layer in Ti_3AlC_2 powder was selectively etched using a LiF/HCl mixed solution to prepare $Ti_3C_2T_x$ MXenes. First, 20 mL of 9 M hydrochloric acid solution was added to a polytetrafluoroethylene vial, followed by the slow addition of 1 g of LiF under magnetic stirring (500 rpm). Then, 1 g of Ti_3AlC_2 powder was added, and the reaction was carried out at 40 °C for 24 h. After the reaction, the product was collected by centrifugation and repeatedly washed with deionized water until neutral (pH = 7). The resulting precipitate was dispersed in 100 mL of deionized water and subjected to ultrasonic treatment for 1 h under argon (Ar) protection to promote delamination. The undelaminated residues were removed by low-speed centrifugation, obtaining a delaminated $Ti_3C_2T_x$ (d-$Ti_3C_2T_x$) suspension. To enhance the dispersibility of d-$Ti_3C_2T_x$ in DMSO, surface modification was further performed using tetrabutylammonium hydroxide (TBAOH). Specifically, 1 g of d-$Ti_3C_2T_x$ powder was mixed with 24 mL of TBAOH solution and stirred at room temperature for 4 h. The mixture was then washed with ethanol to remove free TBAOH, and the precipitate was collected and vacuum-dried at 80 °C for 24 h, finally obtaining the surface-modified $Ti_3C_2T_x$ MXene.

2.3. Preparation of Kevlar nanofiber (KNF) dispersion

Deprotonation of the amide bonds of aramid fibers (Kevlar) was achieved through a mixed system of KOH and DMSO, reducing intermolecular hydrogen bonding and chain stiffness, thereby obtaining Kevlar nanofibers at the nanoscale.[27] Specifically, 2.0 g of Kevlar fibers, 2.0 g of KOH, and 98.0 g of DMSO were mixed in a sealed container, and magnetically stirred at room temperature for 7 days, ultimately forming a deep red dispersion of Kevlar nanofibers.

2.4. Preparation of MXene/SiO_2/KNF aerogels (MSKAs)

A sustained-release gel agent (SRGA) was prepared by mixing dimethyl sulfoxide (DMSO), ethyl acetate (EA), and deionized water (DI) in a mass ratio of 7 : 2 : 1. Subsequently, different masses of MXenes (0.5, 1.0, 1.5 g) were added to 5 mL of SRGA along with 0.2 g of SiO_2 aerogel particles, and the mixture was sonicated until uniform dispersion was achieved. Next, 5 mL of KNF dispersion was added and vigorously stirred to form a homogeneous mixture. The mixture was then injected into molds for gelation and aging, followed by multiple rinses with deionized water to remove residual surfactants and other chemicals. Then, solvent exchange was performed using a water/*tert*-butanol mixture (mass ratio 1 : 1), with three sequential exchanges, each lasting one day. After completion, the gel was frozen in a refrigerator. It was then subjected to freeze-drying at −40 °C for 48 h to obtain the aerogel. Finally, the aerogel was thermally treated at 450 °C for 30 minutes under an argon atmosphere to achieve thermal crosslinking. Through this process, MXene/SiO_2/KNF aerogels (MSKAs) were obtained, named MSKA-1, MSKA-2, and MSKA-3 according to the MXene content (0.5, 1.0, and 1.5 g). For comparison, pure Kevlar nanofiber aerogels (KNFAs) and SiO_2/KNF composite aerogels (SKAs) were prepared using the same method.

2.5. Characterization

The phase composition of the samples was characterized using X-ray diffraction (XRD, Haoyuan, DX-2700BH). Chemical composition information was obtained by laser Raman spectroscopy (Witec Alpha300, λ = 532 nm) and Fourier transform infrared (FTIR) spectroscopy (Nicolet 380). The elemental composition and chemical bonding states of the samples were determined using X-ray photoelectron spectroscopy (XPS). The microstructure, morphology, and elemental distribution of the samples were observed using a field emission scanning electron microscope (SEM, FEI Sirion 200) and energy dispersive spectrometer (EDS). The specific surface area and pore size distribution of the samples were measured by the Brunauer–Emmett–Teller (BET) method using a physical adsorption analyzer (ASAP 2460, Micromeritics) by analyzing nitrogen adsorption and desorption isotherms. The thermal insulation performance of the aerogels was assessed using thermocouples

(JK808, Changzhou Jinailian Co., Ltd) and an infrared camera (TiX580, Fluke). The electromagnetic parameters were measured using a vector network analyzer (ANRITSU MS46322B) with a frequency range of 2–18 GHz. To evaluate the electromagnetic properties of the material, the aerogel was immersed in molten paraffin and compressed into a ring-shaped sample with an outer diameter of 7.00 mm and an inner diameter of 3.04 mm. These parameters included the complex permittivity ($\varepsilon_r \approx \varepsilon' - j\varepsilon''$) and complex permeability ($\mu_r \approx \mu' - j\mu''$). The electromagnetic wave absorption capability represented by RL, attenuation constant (α), $\lambda/4$ resonance model (t_m), the normalized wave impedance (η) and interface reflection coefficient (R) were calculated according to the transmission line theory using the following formulas:[30–32]

$$\mathrm{RL\ (dB)} = 20\lg\left|\frac{Z_{in} - Z_0}{Z_{in} + Z_0}\right| \quad (1)$$

$$Z_{in} = Z_0\sqrt{\frac{\mu_r}{\varepsilon_r}}\tanh\left(j\frac{2\pi fd}{c}\sqrt{\mu_r\varepsilon_r}\right) \quad (2)$$

$$\alpha = \frac{\sqrt{2}\pi f}{c} \times \sqrt{(\mu''\varepsilon'' - \mu'\varepsilon') + \sqrt{(\mu'\varepsilon'' + \mu''\varepsilon')^2 + (\mu''\varepsilon'' - \mu'\varepsilon')^2}} \quad (3)$$

$$t_m = \frac{nc}{4f_m\sqrt{|\varepsilon_r||\mu_r|}} \quad (n = 1, 3, 5, \ldots) \quad (4)$$

$$\eta = \sqrt{\frac{\mu_r}{\varepsilon_r}} \quad (5)$$

$$R = \left|\frac{\sqrt{\frac{\mu_r}{\varepsilon_r}} - 1}{\sqrt{\frac{\mu_r}{\varepsilon_r}} + 1}\right|^2 \quad (6)$$

here, Z_{in} represents the input impedance, Z_0 denotes the free-space impedance (Z_0 = 376.7 Ω), c signifies the speed of light in a vacuum, f represents the EMW frequency, d stands for the thickness of the absorbing material, and j is the imaginary unit. The attenuation constant α represents the rate at which electromagnetic waves are attenuated as they propagate through the material. It quantifies the energy loss of the waves during propagation, which can be used to describe the extent to which the material absorbs electromagnetic waves.

2.6. RCS simulation

The radar cross-section (RCS) of the MSKA under realistic far-field conditions was simulated using CST Studio Suite 2020. The simulation model featured a double-layer panel measuring 20 cm × 20 cm, comprising a 1.83 mm-thick MSKA-2 aerogel absorption layer on top of a 1.0 mm-thick perfect electric conductor (PEC) layer. The model was oriented in the X–O–Y plane and irradiated with a plane electromagnetic wave propagating along the negative Z-axis. The angular range of incidence was varied from −60° to 60°. Open boundary conditions were imposed in all directions to replicate far-field effects. The RCS was calculated using the following equation:

$$\sigma(m^2) = \lim_{R\to\infty} 4\pi R^2\left(\left|\frac{E_s}{E_i}\right|\right)^2 = \lim_{R\to\infty} 4\pi R^2\left(\left|\frac{H_s}{H_i}\right|\right)^2 = \lim_{R\to\infty} 4\pi R^2\frac{S_s}{S_i} \quad (7)$$

here, the term $\lim_{R\to\infty}$ represents the limit as the radial distance R approaches infinity, ensuring analysis in the far-field region. The factor $4\pi R^2$ corresponds to the surface area of a sphere with radius R, accounting for the distribution of scattered energy over the spherical surface. The quantities $|E_s|$ and $|H_s|$ denote the magnitudes of the scattered electric and magnetic fields, respectively, with their squared values ($|E_s|^2$ and $|H_s|^2$) proportional to the energy density of the scattered wave. S_s represents the scattered power flux density (the rate of energy transfer per unit area due to the scattered wave), while S_i denotes the incident power flux density (the same for the incoming wave). The ratio S_s/S_i defines the scattering efficiency, a dimensionless quantity that measures the fraction of incident power scattered by the object.

3. Results and discussion

3.1. Microstructure and the chemical composition

The preparation process of MXene/SiO_2/KNF aerogels (MSKAs) involves four steps: chemical fiber exfoliation, slow-release gelation, freeze-drying, and high-temperature heat treatment (Fig. 1a). First, Kevlar fibers are chemically exfoliated and deprotonated using a KOH/DMSO system to obtain a uniform and stable KNF dispersion. Subsequently, MXene dispersion and SiO_2 aerogel particles are added to a slow-release gelator composed of EA, DI, and DMSO. During this process, EA slowly decomposes into acetic acid and ethanol. According to the protonic acid–base theory proposed by Brønsted and Lowry,[33] the generated acetic acid and ethanol, as proton donors, promote the self-assembly behavior of deprotonated KNF, leading to the formation of a 3D network structure through hydrogen bond reconstruction and inducing gelation (Fig. 1b). After gelation, a deionized water/*tert*-butanol (1 : 1, w/w) solvent exchange system is used to remove residual DMSO and KOH, while the cosolvent effect suppresses the collapse of the aerogel structure during freeze-drying.[27] Finally, after annealing at 450 °C in an argon atmosphere for 30 minutes, unstable components in the system are removed, and thermal cross-linking between nanofibers is achieved, resulting in a series of samples. This process provides excellent control over the gelation process, allowing compatibility with molding and extrusion methods to obtain aerogels in various forms such as bulk and fibers (Fig. 1c). The prepared MSKA composite aerogel exhibits ultra-low density (5–30 mg cm^{-3}), can be gently placed on the surface of a dandelion fluff without causing deformation (Fig. 1d), and demonstrates excellent mechanical properties, capable of bearing a load 1000 times its own weight without structural damage (Fig. 1e).

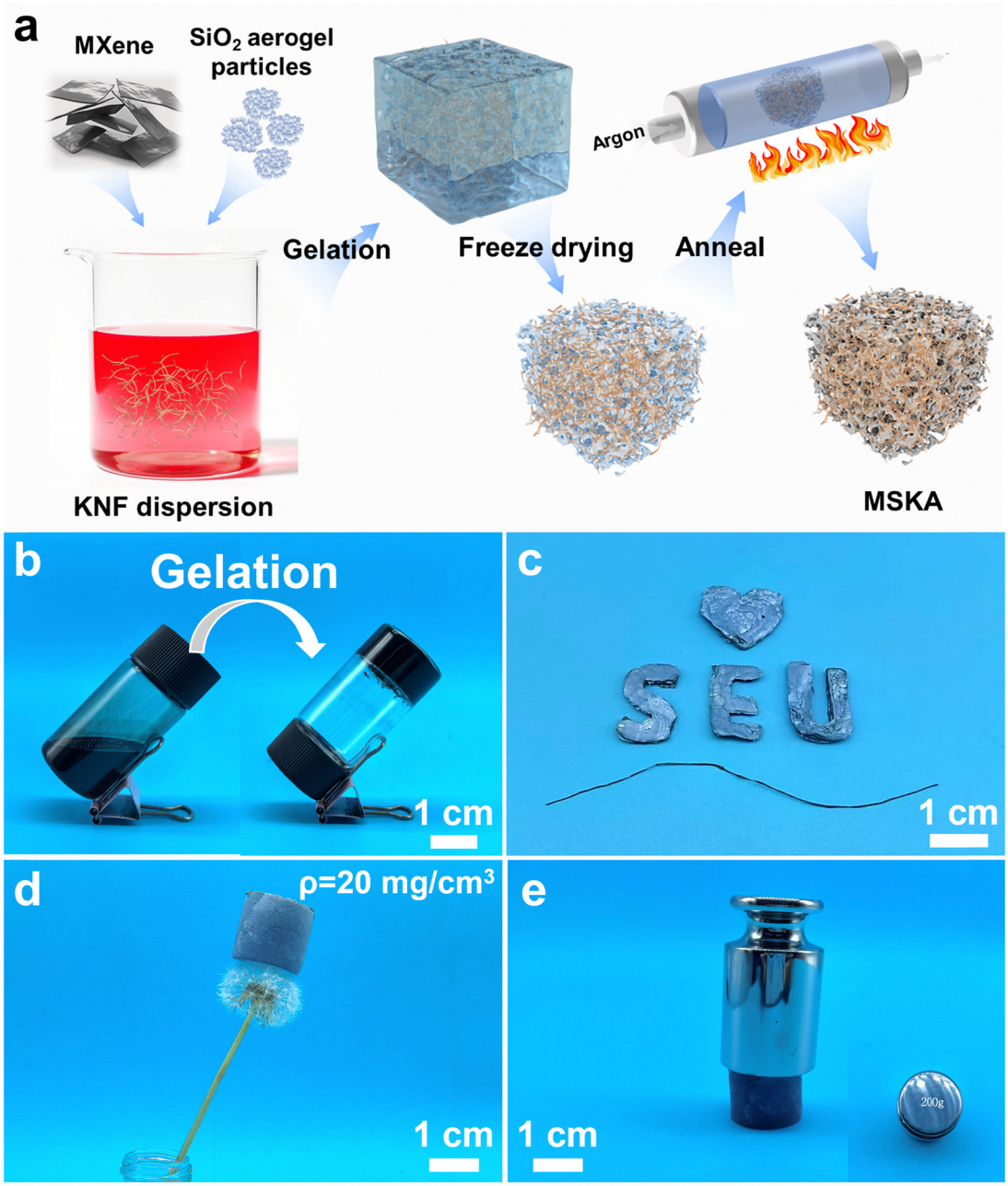

Fig. 1 Preparation and physical images of MSKA: (a) Schematic diagram of the preparation process; (b) images of the gelation process; (c) photographs of MPKA-2 molded into blocks and fibers; (d) ultra-low density demonstration of MPKA-2 placed on the surface of a dandelion fluff; and (e) mechanical performance demonstration of MPKA-2 bearing a 200 g weight.

Fig. 2a shows the X-ray diffraction (XRD) patterns of MXene, MSKA-2, KNFA, and SiO_2 aerogel particles. The characteristic diffraction peaks of KNFA at 20.8°, 23.3°, and 28.5° correspond to the (110), (200), and (004) crystal planes,[28] respectively, while the diffraction peak of $Ti_3C_2T_x$ MXene at 6.7° is attributed to the (002) crystal plane. Notably, the (002) crystal plane peak in MSKA-2 shifts to a lower angle by 0.7° compared to pure MXene, indicating an expansion of the interlayer spacing.[34,35] This may be due to the introduction of KNF nanofibers into the interlayers of MXene nanosheets, effectively inhibiting the self-stacking of the nanosheets.[36] Additionally, the broad diffraction peak of the SiO_2 aerogel at ~23° confirms its amorphous structure.[37] MSKA-2 exhibits characteristic peaks of both MXene, KNFA, and SiO_2 aerogel, confirming the successful construction of the composite system. The Fourier transform infrared (FTIR) spectroscopy in Fig. 2b shows that the characteristic peaks of MXene at 3480 and 1661 cm^{-1} correspond to the –OH stretching vibrations and C–O bond vibrations, respectively,[38] while the peaks of KNFA at 3327 cm^{-1} and 1649 cm^{-1} arise from the N–H stretching vibrations and amide

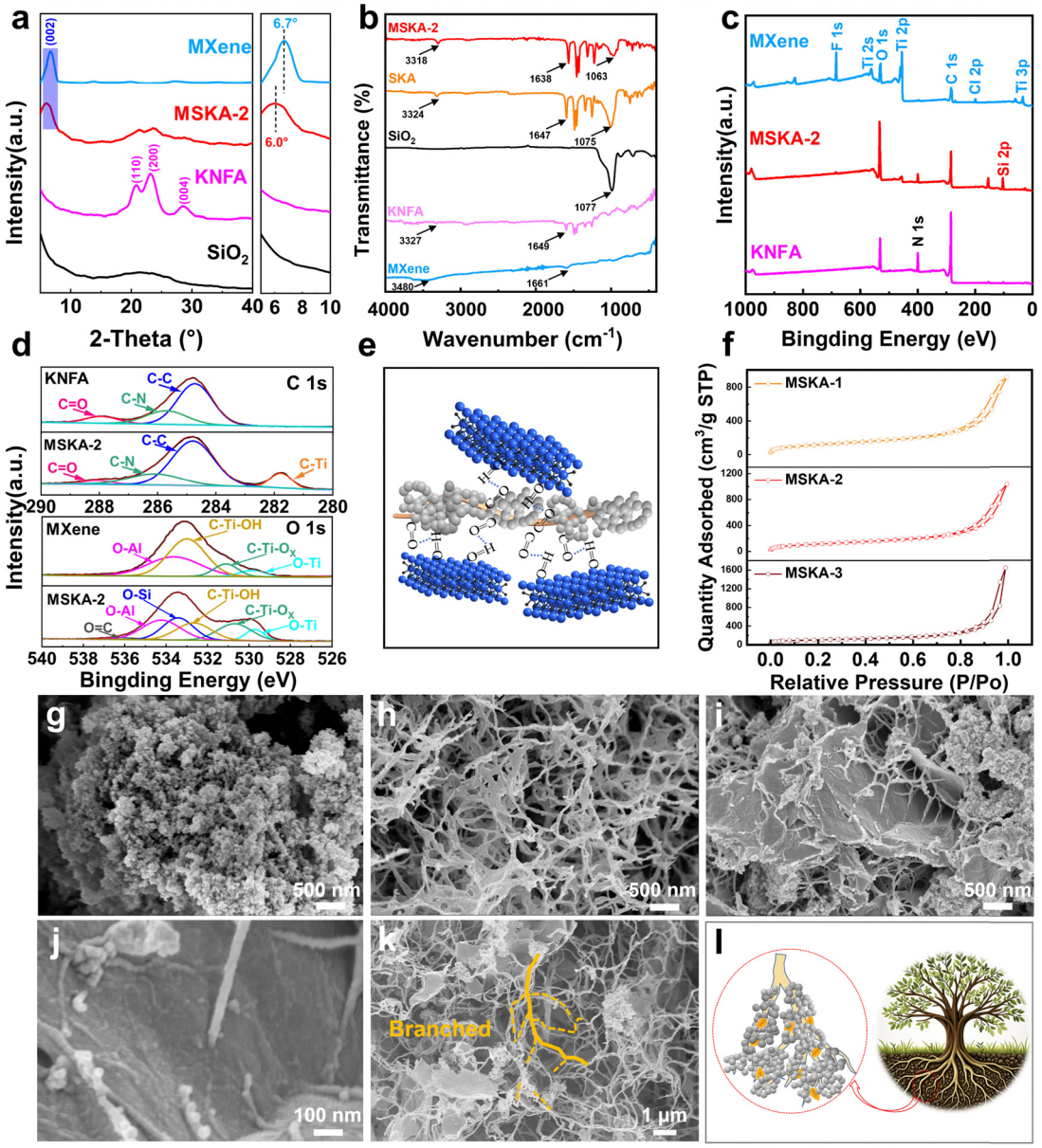

Fig. 2 Structural and morphological characterization of MSKAs: (a) XRD spectra, (b) FTIR spectra, and (c) XPS full spectra of MXenes, MSKA-2, KNFA, and SiO_2; (d) high-resolution C 1s spectra of MSKA-2 and KNFA, and high-resolution O 1s spectra of MSKA-2 and MXenes; (e) Schematic illustration of the binding mechanism between components in MSKA-2; (f) N_2 adsorption–desorption isotherms of the samples MSKA; SEM images of (g) SiO_2 aerogel particles, (h) KNFA, and (i)–(k) MSKA-2; and (l) schematic illustration of the biomimetic "root–soil" structure.

C═O stretching vibrations, respectively.[39] The presence of hydrogen bonds can be clearly observed from the changes in C═O vibrational energy. In MSKA-2, the C═O vibration peak shifts from 1649 cm^{-1} to 1638 cm^{-1}, indicating the hydrogen bond competition between the –F/–OH functional groups of MXene and the C═O groups, leading to changes in electron density.[40] Simultaneously, the N–H stretching vibration peak shifted from 3327 cm^{-1} to 3318 cm^{-1}, and the asymmetric stretching vibration peak of Si–O–Si shifted from 1077 cm^{-1} to 1063 cm^{-1}. These spectral changes suggest the formation of hydrogen bonds between the N–H groups of KNFs and the Si–O groups of silica, validating the interfacial interactions in the composite system.[41,42] X-ray photoelectron spectroscopy (XPS) analysis (Fig. 2c) confirms that MSKA-2 contains Ti, C, F, Cl, O, N, and Si elements. The C 1s spectrum of KNFA shows peaks at 287.9 eV, 285.8 eV, and 284.7 eV, corresponding to C═O, C–N, and C–C bonds, respectively. The C 1s spectrum of MSKA-2, in addition to retaining the above peaks, also shows a Ti–C bond signal at 281.8 eV (Fig. 2d), corresponding to the typical chemical state of MXene. For the O 1s spectrum, the peaks of MXenes at 533.6 eV, 533.0 eV, 531.1 eV, and 529.8 eV correspond to O–Al, C–Ti–OH, C–Ti–O_x, and O–Ti bonds, respectively. In contrast, the O 1s spectrum of MSKA-2 shows additional peaks at 533.4 eV (O–Si) and 536.3 eV (O═C),

attributed to SiO_2 and KNF, respectively.[43] Notably, the C═O peak in MSKA-2 shifts to higher binding energy (287.9 → 288.08 eV), while the C–Ti–OH peak shifts to lower binding energy (533.02 → 532.66 eV), indicating hydrogen bond competition between the –F/–OH groups on the MXene surface and the C═O groups of KNF, leading to a decrease in C═O electron density, consistent with the FTIR redshift results.[44] The above spectroscopic evidence collectively validates the hydrogen bond interactions between KNFs and SiO_2/MXenes, with the binding mechanism illustrated in Fig. 2e. Moreover, an analysis of the composition in Table S1 (ESI†) using XPS and EDS reveals that the proportion of O element in the sample MSKA-2 is slightly higher than the theoretical value, suggesting the presence of some degree of oxidation on the sample surface. Nevertheless, the overall composition remains consistent with the designed values, which not only validates the rationality of the experimental design but also demonstrates the good chemical stability and structural controllability of MSKA-2 during the preparation process. N_2 adsorption analysis (Fig. S1, ESI†) reveals that MXene exhibits a relatively low specific surface area of only 8.6 $m^2\ g^{-1}$ due to its densely stacked layered structure, significantly lower than that of the fibrous KNF (182 $m^2\ g^{-1}$) and the highly porous SiO_2 aerogel (647 $m^2\ g^{-1}$). With an increase in the MXene content, the specific surface area of the MSKA composites shows a slight decreasing trend overall. The specific surface area of MSKA-2 is 427 $m^2\ g^{-1}$, falling between those of MSKA-1 (437 $m^2\ g^{-1}$) and MSKA-3 (358 $m^2\ g^{-1}$) (Fig. 2f), indicating that the appropriate incorporation of MXene helps maintain a favorable pore structure while still achieving a relatively high surface area. The average pore size of MSKA-2 is 14.9 nm, which is lower than that of pure SiO_2 aerogel (28.3 nm), suggesting that the MXene nanosheets may synergistically fill certain pore spaces, leading to a moderate reduction in overall pore size.[41] Notably, despite the decrease in specific surface area caused by the addition of MXene, MSKA-2 still retains a high surface area and a well-distributed pore structure, demonstrating that the three-dimensional porous network remains largely intact. This highlights the good structural compatibility and synergistic construction capability among the composite components.

Scanning electron microscopy (SEM) revealed the microstructures of aerogel samples such as SiO_2, KNFA, and MSKA-2 (Fig. 2g–k). The SiO_2 aerogel consists of a 3D porous framework formed by interconnected nanoparticles (Fig. 2g), with an average pore size close to the mean free path of air molecules, indicating that such a pore structure can effectively restrict gas molecule movement and thus enhance thermal insulation.[45] The SEM image of KNFA (Fig. 2h) shows that Kevlar nanofibers (KNF) form a 3D cross-linked network through physical entanglement and hydrogen bonding, with a uniform distribution of fiber diameters. In MSKA-2, the KNF skeleton links MXene nanosheets and SiO_2 particles into an integrated 3D network (Fig. 2i), where the KNF and MXene interfaces are tightly connected (Fig. 2j), a bonding attributed to hydrogen bonding between the two (as described by FTIR and XPS analyses). Fig. 2k more clearly shows the biomimetic ''root–soil'' structure formed by branched fibers and nanoscale SiO_2 particles through hydrogen bonding. Furthermore, a comparative analysis of the EDS mapping of SiO_2 (Fig. S2, ESI†), KNFA (Fig. S3, ESI†), SKA (Fig. S4, ESI†), and MSKA-2 (Fig. S5, ESI†) reveals that Si, O, and Ti elements are distributed in significant agglomerated forms within the KNF network, while C and N exhibit a homogeneous spatial distribution. These elemental distribution characteristics provide strong evidence for the existence of a ''root–soil'' structure in the MSKA. This structure enhances particle bonding through multi-directional anchoring, analogous to the mechanism of root systems stabilizing soil in nature, as shown in Fig. 2l. Compared to traditional 3D networks, such bionic structures exhibit higher strength and toughness due to the multi-directional stress dispersion mechanism of branched fibers. This is because the uniform stress distribution in 3D space can suppress local fatigue failure, while the multi-level anchoring effect effectively impedes crack propagation, resulting in superior durability under cyclic loading. Through hydrogen bonding, branched KNF anchors SiO_2 particles and MXene nanosheets into a 3D continuous network, significantly enhancing the mechanical properties of the MSKA composite aerogel (Fig. S6, ESI†).[46,47]

3.2. Electromagnetic wave absorption performance

The real part (ε') and imaginary part (ε'') of the dielectric constant of electromagnetic absorption materials represent the material's ability to store and dissipate electrical energy in the electric field component of electromagnetic waves, respectively.[22] Since all samples in this study exhibit no magnetic response characteristics, the real part (μ') and imaginary part (μ'') of the permeability are consistently 1 and 0, respectively. As shown in Fig. S7a and b (ESI†), pure MXene exhibits an extremely high dielectric constant, with peak values of ε' and ε'' reaching 65.0 and 60.1, respectively. However, this highly conductive material is prone to severe impedance mismatch effects, causing strong reflection of incident electromagnetic waves at the surface and making it difficult for the waves to penetrate the material. In contrast, the dielectric constant of SKA is very low, with a peak ε' of 2.4 and a peak ε'' of 0.3, indicating that this material has almost no attenuation effect on electromagnetic waves. By adjusting the content of MXene relative to KNFs and SiO_2 in the composite system, the dielectric constant was effectively controlled. The ε' and ε'' of MSKA-1 were controlled within the ranges of 6.7–12.6 and 2.4–5.3, respectively, while MSKA-2 was further optimized to 4.6–13.8 (ε') and 2.0–6.1 (ε''). Compared to other samples, MSKA-2 and MSKA-3 samples exhibited higher dielectric loss tangent values ($\tan\delta_\varepsilon$) and attenuation constants (α) across the entire test frequency range, indicating their excellent electromagnetic loss capabilities (Fig. S7c and d, ESI†). Notably, the MSKA series samples showed significant fluctuations in dielectric constant across the test frequency band, primarily due to the synergistic effects of interfacial polarization and dipole relaxation, which induce multiple relaxation peaks.[48,49]

By comparing the electromagnetic wave absorption performance of MXene, SKA, and MSKA samples (Fig. S8 (ESI†) and

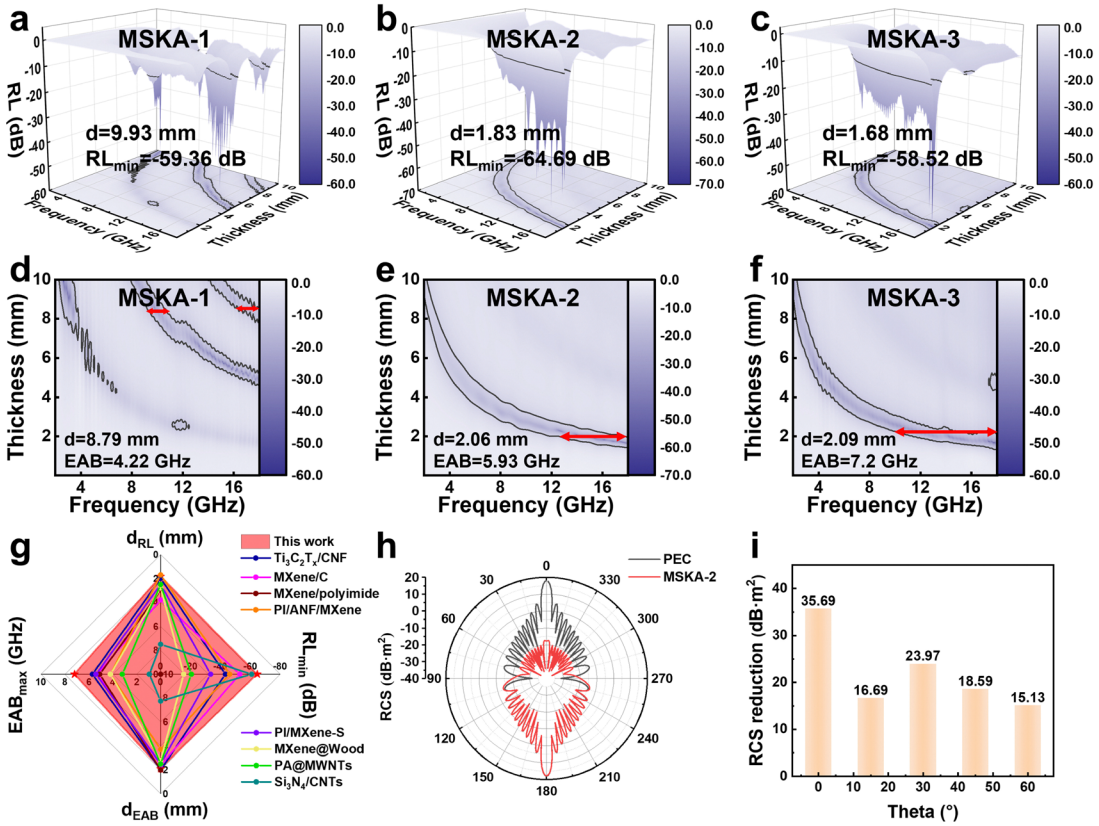

Fig. 3 Electromagnetic wave absorption performance and application verification of MSKA: (a)–(c) 3D RL values and (d)–(f) 2D RL values of MSKA-1, MSKA-2, and MSKA-3; (g) comprehensive comparison of RL values and EAB for other materials reported in the literature;[34,35,50–56] (h) full-angle RCS simulation results of the PEC substrate coated with MSKA-2 and the bare PEC substrate; and (i) the simulation results of PEC and MSKA-2 at −60 to 60° scattering angle.

Fig. 3a–f), the intrinsic relationship between material structure and electromagnetic response was revealed. Although pure MXene has a high dielectric loss, its strong conductivity-induced impedance mismatch effect leads to an increase in electromagnetic wave reflectivity, with the minimum reflection loss value (RL_{min}) reaching only −38.19 dB, and the effective absorption bandwidth (EAB, RL < −10 dB) being only 2.07 GHz (Fig. S8a and b, ESI†). Due to the insufficient dielectric loss capability of the SiO_2/KNF composite aerogel (SKA), its RL_{min} value is only −5.12 dB, indicating negligible electromagnetic wave absorption performance (Fig S7c and d, ESI†). After constructing a ''root–soil'' structure through bionic design, MSKA exhibited significantly optimized wave absorption performance. Limited by its weaker dielectric loss capability, MSKA-2 only achieved an EAB value of 4.22 GHz at a high thickness of 8.79 mm. In contrast, the RL_{min} value of MSKA-2 was improved to −64.69 dB, corresponding to a matching thickness of 1.83 mm, while MSKA-3 achieved an RL_{min} of −58.52 dB at a thickness of 1.68 mm. More notably, the EAB values of MSKA-2 and MSKA-3 reached 5.93 GHz and 7.2 GHz, respectively, significantly outperforming SKA and pure MXene. As shown in Fig. 3g, compared with other electromagnetic wave absorbing materials reported in the literature, the MSKA prepared in this study exhibits a superior RL_{min} (minimum reflection loss) and a broader EAB_{max} (maximum effective absorption bandwidth) at a relatively lower thickness.[34,35,50–56] This excellent performance is mainly attributed to its unique hierarchical heterogeneous interface structure, which significantly enhances the material's absorption performance by synergistically optimizing impedance matching and electromagnetic attenuation.

To verify the actual radar stealth performance of MSKA, finite element simulation analysis was conducted to evaluate its radar cross-section (RCS) as an absorbing coating under far-field conditions. As shown in Fig. 3h, the maximum RCS value of an uncoated perfect electric conductor (PEC) substrate at a 0° incident angle is 18.0 dB m^2. In contrast, the PEC substrate coated with MSKA-2 reduces the RCS to −17.69 dB m^2 under the same conditions, resulting in a total RCS reduction of 35.69 dB m^2 (Fig. 3i). This performance not only significantly surpasses the military stealth technology requirement of 10 dB m^2 but also outperforms other materials such as MXene (4.4 dB m^2) or SKA (0.9 dB m^2) (Fig. S9, ESI†).[57] The full-angle scattering analysis further indicates that the MSKA-2 coating maintains excellent RCS suppression performance over a wide range of angles. The experimental results are highly consistent with the conclusions from the preceding electromagnetic parameter analysis, confirming that MSKA-2 effectively dissipates incident electromagnetic wave energy through the synergistic

effect of multilevel heterogeneous interface polarization and conduction loss, demonstrating significant application potential in wideband and multi-angle radar stealth applications.

3.3. Electromagnetic wave absorption mechanism

Additionally, this study further revealed the intrinsic mechanism behind the superior electromagnetic wave absorption performance of MSKA compared to other samples by analyzing the impedance matching capabilities of each sample. Fig. 4a–c and Fig. S10 (ESI†) compare the frequency domain characteristics of the normalized wave impedance (η) and interface reflection coefficient (R) of MSKA, MXene, and SKA samples. Compared to MXene, the η values of the MSKA series samples were closer to the ideal matching value of 1 across the entire test frequency range, and their R values were significantly lower than those of MXene. This characteristic indicates that MSKA materials have lower reflectivity of incident electromagnetic waves at the air–material interface, thereby offering better impedance matching conditions. According to electromagnetic wave absorption theory, the ideal normalized impedance value (Z) is a key factor in ensuring the penetration of electromagnetic waves into the material. Impedance mismatch will cause electromagnetic waves to reflect at the material surface and fail to be effectively dissipated. Therefore, a more intuitive comparison of Z values among the samples was conducted. As shown in Fig. S11a (ESI†), the 2D distribution of Z values for MXene reveals that the area of its ideal impedance matching region ($0.8 \leq Z \leq 1.2$) is only 1.71%, indicating significant impedance mismatch, primarily due to the excessively high dielectric constant of MXene, which causes significant reflection of electromagnetic waves at the material surface.[58] In contrast, the impedance matching performance of the MSKA series samples was significantly improved (Fig. 4d–f), resulting from the multi-level pore network design inspired by the "root–soil" structure. Although SKA has the largest impedance matching interval (11.86%), its electromagnetic wave absorption capability is extremely poor due to the lack of electromagnetic attenuation mechanisms (Fig. S11b, ESI†). For the MSKA series composite aerogels, the 3D interconnected pores serve as electromagnetic wave transmission channels, promoting the penetration of electromagnetic waves into the material through refraction and scattering effects. The hierarchical porous structure generates interfacial polarization effects, enhancing multiple internal reflections of electromagnetic waves and extending the energy dissipation path. The introduction of low-dielectric components such as KNFs and SiO_2 effectively regulates the dielectric constant of the composite, making its characteristic impedance closer to the free space impedance.[25] This synergistic

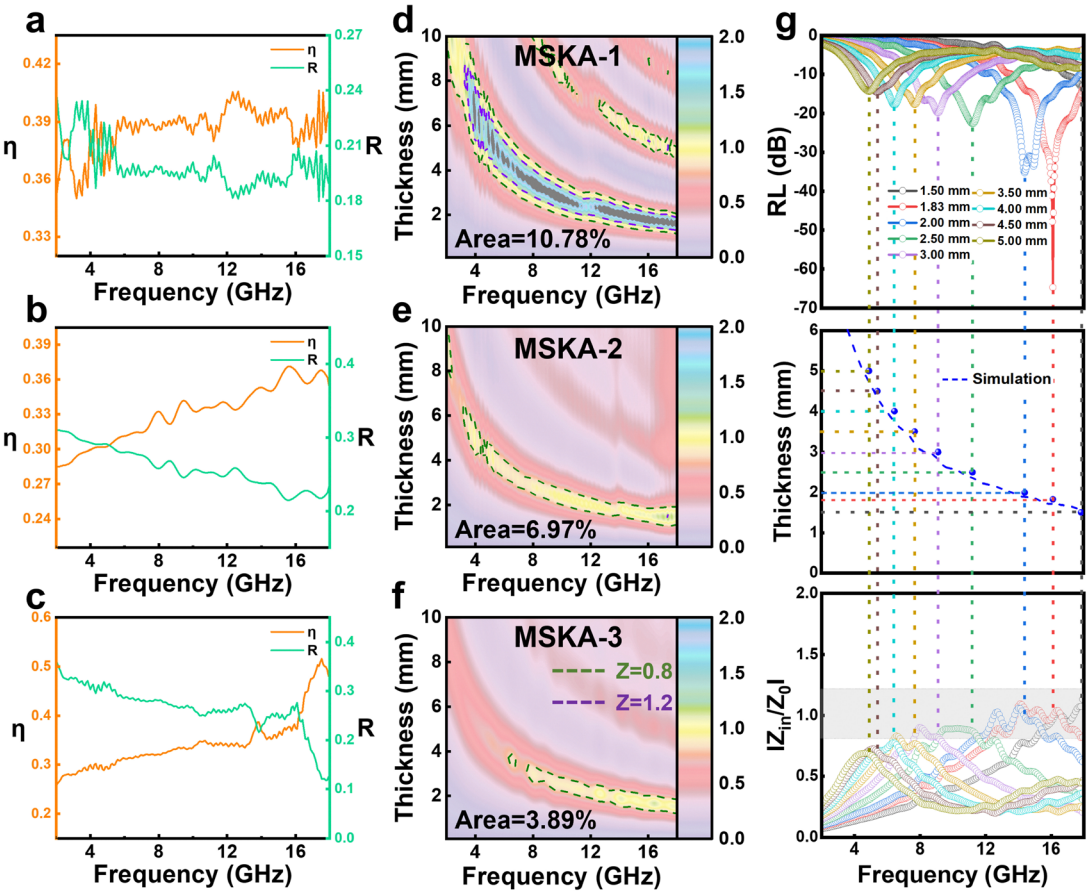

Fig. 4 Analysis of impedance matching characteristics of MSKA: normalized wave impedance η and interface reflection coefficient R curves of (a) MSKA-1, (b) MSKA-2, and (c) MSKA-3, along with (d)–(f) visualized 2D impedance matching diagrams; and (g) RL, t_m, and Z values of MSKA-2 in the $\lambda/4$ model.

effect is further validated in Fig. 4d, where the minimum reflection loss values of MSKA-2 correspond to the matching condition of $Z \approx 1$. Moreover, as the sample thickness increases, the RL peak shifts to lower frequencies, in line with the $\lambda/4$ resonance model (formula (4)),[59,60] indicating that the material can effectively capture and attenuate electromagnetic waves in specific frequency bands through thickness regulation.[61,62]

This study reveals the electromagnetic wave attenuation mechanism of the MXene/SiO_2/KNF composite aerogel (MSKA) through a cross-dimensional integration strategy (Fig. 5). Firstly, a biomimetic "root–soil" structure efficiently captures and dissipates electromagnetic waves through a multi-level pore network. The 3D porous framework serves as a channel for electromagnetic wave transmission, guiding waves deep into the material through refraction and scattering effects, significantly reducing surface reflectivity.[6] Secondly, the introduction of low-dielectric components KNFs and SiO_2 effectively tunes the high dielectric response of MXene, enhancing the material's characteristic impedance match with free space impedance, thereby optimizing the efficiency of electromagnetic wave incidence. Additionally, the stacked structure of two-dimensional MXene nanosheets within the material induces interfacial polarization effects, leading to multiple reflection behaviors that extend the propagation path of electromagnetic waves inside the material and promote energy dissipation.[63] Notably, the 3D conductive network constructed between MXene layers generates directional electron migration under electromagnetic field excitation, converting electromagnetic energy into thermal energy through Joule heating effects,[64] while the abundant surface functional groups and lattice defects further enhance energy loss through dipole polarization mechanisms.[65] Under the synergy of multiple mechanisms, the MSKA composite aerogel exhibits excellent electromagnetic wave absorption performance.

To systematically evaluate the infrared stealth properties of aerogel samples such as KNFA, SKA, and MSKA-2, this study conducted high-temperature experiments using 1.5 cm thick samples on a 175 °C heating platform and monitored the dynamic changes in the surface temperature of the materials in real time using infrared thermal imaging technology. The infrared thermal imaging results showed that under the condition of the heating platform temperature stabilizing at 175 °C, the maximum surface temperatures of KNFA, SKA, and MSKA-2 reached 91.0 °C, 61.4 °C, and 52.2 °C, respectively, forming significant temperature gradients of 83.4 °C, 116.0 °C, and 123.1 °C (Fig. 6a_1–a_3). Among them, MSKA-2 exhibited the most excellent thermal insulation performance, a conclusion further verified by the comparative analysis in Fig. 6a_4. Notably, the thermal infrared image of the handheld MSKA-2 sample showed a surface color similar to the environmental background, directly confirming the material's good compatibility with infrared stealth (Fig. 6b). Through the temperature-time curve analysis, it was found that after reaching thermal equilibrium at 200 seconds, the heating platform eventually stabilized at 150 °C, while the surface temperatures of KNFA, SKA, and MSKA-2 remained at 60 °C, 45 °C, and below 40 °C, respectively. In particular, the SiO_2 aerogel particles introduced in the SKA sample significantly enhanced the thermal insulation efficiency by inhibiting air convection within the fiber matrix, and the composite modification with MXene nanosheets further expanded the temperature gradient of MSKA-2 to over 110 °C, demonstrating excellent thermal barrier properties (Fig. 6c). Additionally, in the composite aerogel system containing organic components, flame retardancy, as a key safety indicator, can significantly reduce personnel safety risks and thermal damage to electronic devices in fire scenarios by inhibiting material combustion.[66] The flame retardancy test based on a butane flame showed that MSKA-2 had a rapid self-extinguishing characteristic (Fig. 6d_1–d_3), which was attributed to the synergistic effect of the high content of non-flammable SiO_2 aerogel particles inside and the inherent flame-retardant

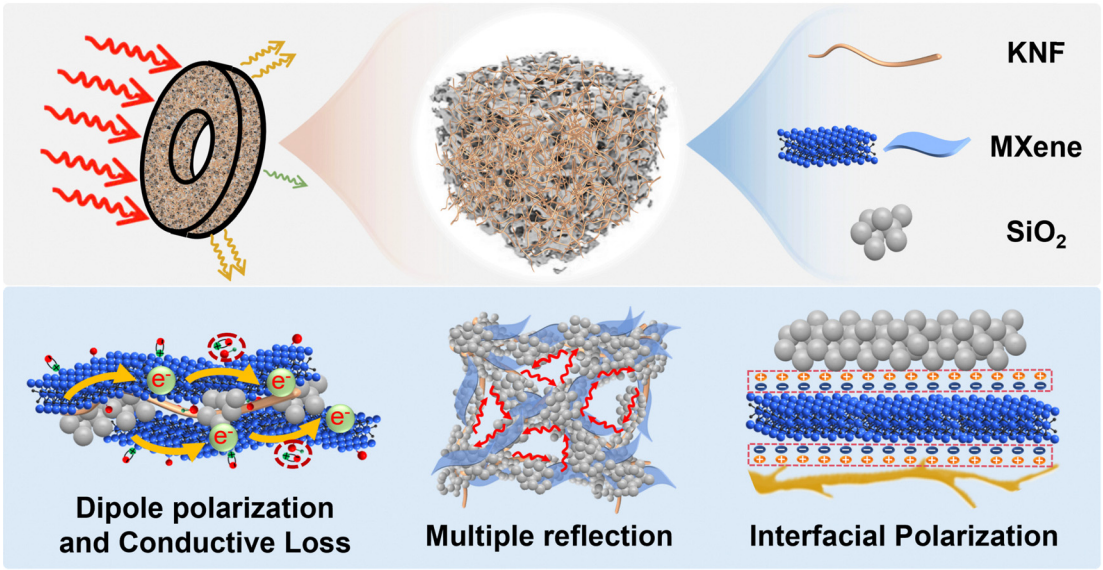

Fig. 5 Schematic diagram of the electromagnetic wave absorption mechanism of MSKAs.

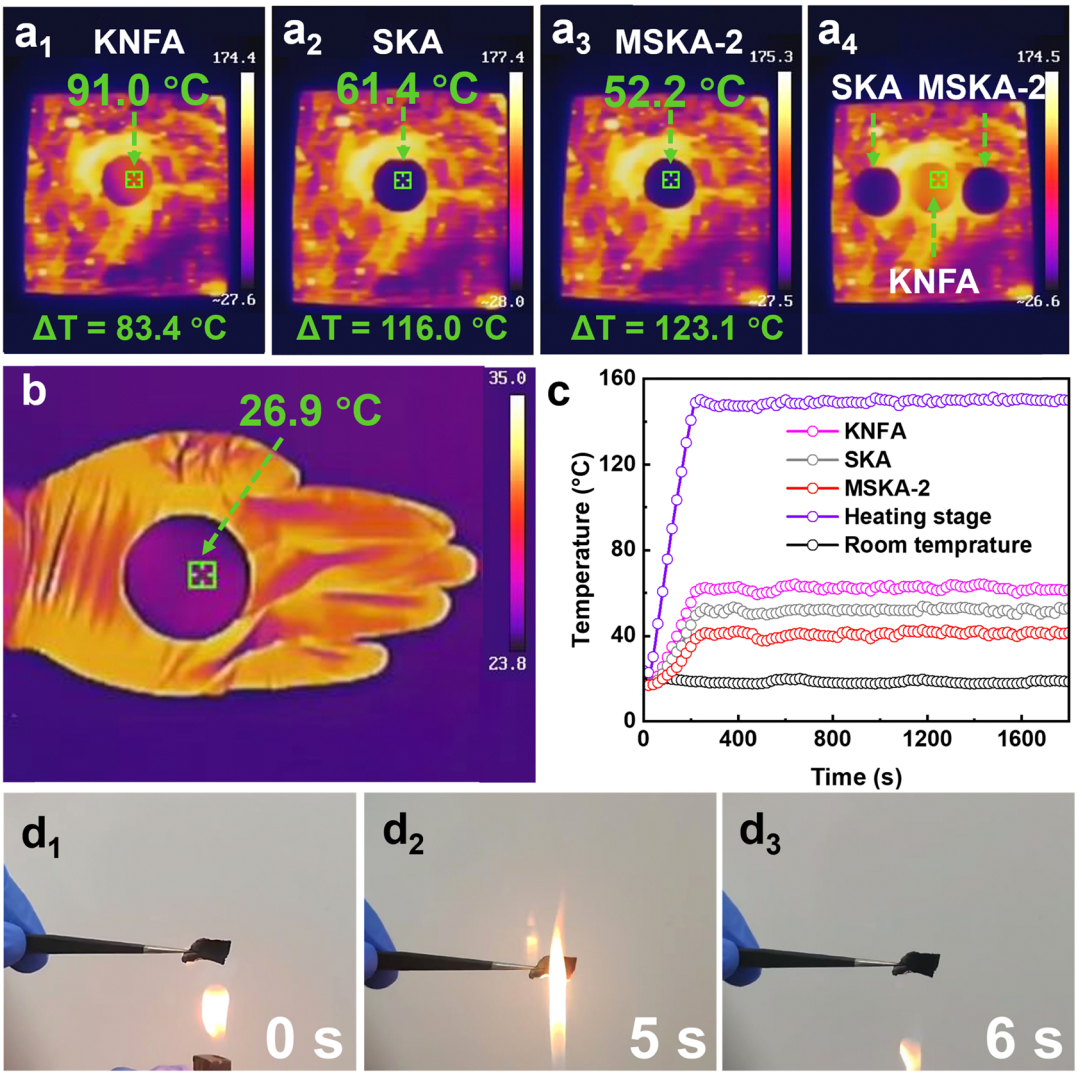

Fig. 6 (a) Thermal infrared images of KNFA, SKA, and MSKA-2 on a 175 °C heating platform; (b) thermal infrared image of MSKA-2 placed on a hand; (c) surface temperature variation curve of MSKA-2 on a 150 °C heating platform; and (d) demonstration of the flame retardant properties of MSKA-2.

properties of KNF. This composite structural design not only endows the material with excellent thermal stability but also provides a reliable fire barrier for protecting personnel and precision equipment.[67]

4. Conclusions

This study innovatively proposes a cross-dimensional integration strategy, accurately constructing an MXene/SiO_2/Kevlar composite aerogel (MSKA) with bionic-inspired root–soil interlocking structures *via* the improved sol–gel method. This design utilizes a hydrogen bonding network to assemble 1D Kevlar nanofibers (KNFs), 2D MXene nanosheets, and 0D SiO_2 aerogel particles, fully leveraging the synergistic effects of components across various dimensions. This achieves breakthroughs in electromagnetic wave absorption and infrared stealth performance while maintaining an ultra-low density. Benefiting from the unique heterogeneous interface polarization effect, the MSKA exhibits exceptional electromagnetic loss capabilities, with an RL_{min} value of −64.69 dB and an EAB coverage of 7.2 GHz. Radar cross-section (RCS) simulations show a reduction of 35.69 dB m^2 in scattering intensity for metal targets. When the material thickness is 15 mm, a significant surface temperature difference of over 120 °C can be formed at a substrate temperature of 175 °C, combined with the consistency of radiation with environmental background in thermal infrared imaging, verifying its excellent infrared stealth capabilities. This multi-dimensional component synergistic strategy provides a new paradigm for developing lightweight, wide-band, and multi-spectrum compatible advanced stealth materials.

Author contributions

Shuo Zhang: formal analysis, investigation, data curation, validation, and writing – original draft. Fushuo Wu: methodology,

investigation, data curation, and writing – original draft. Feiyue Hu: formal analysis. Peiying Hu: data curation. Miaoping Li: data curation. Peng Zeng: data curation. Peigen Zhang: conceptualization, writing – review & editing, project administration, supervision, and funding acquisition. Tianyu Wang: data curation. Shuangshuang Chen: data curation. Jian Liu: funding acquisition. Longzhu Cai: software. ZhengMing Sun: conceptualization, writing – review & editing, project administration, supervision, and resources.

Data availability

The authors confirm that the data supporting the findings of this study are available within the article and its ESI.† Raw data that support the findings of this study are available from the corresponding author, upon reasonable request.

Conflicts of interest

There are no conflicts to declare.

Acknowledgements

This work was supported by the National Natural Science Foundation of China (52171033, 52431003, and U23A20574).

References

1 Y. Wu, S. Tan, Y. Zhao, L. Liang, M. Zhou and G. Ji, *Prog. Mater. Sci.*, 2023, **135**, 101088.
2 L. Liang, X. Yang, C. Li, R. Yu, B. Zhang, Y. Yang and G. Ji, *Adv. Mater.*, 2024, **36**, 2313939.
3 J. Yang, X. Zhang, X. Zhang, L. Wang, W. Feng and Q. Li, *Adv. Mater.*, 2021, **33**, 2004754.
4 J. Dong, Y. Peng, J. Long, Y. Zhang, Z. Wang, T. Park, Y. Huang and T. Liu, *Adv. Funct. Mater.*, 2023, **33**, 2308426.
5 W. Gu, S. J. Ong, Y. Shen, W. Guo, Y. Fang, G. Ji and Z. J. Xu, *Adv. Sci.*, 2022, **9**, 2204165.
6 Z. Zhao, Y. Qing, L. Kong, H. Xu, X. Fan, J. Yun, L. Zhang and H. Wu, *Adv. Mater.*, 2024, **36**, 2304182.
7 M. Qiao, Y. Tian, J. X. Li, X. He, X. Lei, Q. Zhang, M. Ma and X. Meng, *J. Colloid Interface Sci.*, 2022, **609**, 330–340.
8 S. Tan, S. Guo, Y. Wu, T. Zhang, J. Tang and G. Ji, *Adv. Funct. Mater.*, 2025, **35**, 38.
9 J. Xiao, M. He, B. Zhan, H. Guo, J. Yang, Y. Zhang, X. Qi and J. Gu, *Mater. Horiz.*, 2024, **11**, 5874–5894.
10 J. Li, Z. Xu, T. Li, D. Zhi, Y. Chen, Q. Lu, J. Wang, Q. Liu and F. Meng, *Composites, Part B*, 2022, **231**, 109565.
11 Z. Gao, A. Iqbal, T. Hassan, S. Hui, H. Wu and C. M. Koo, *Adv. Mater.*, 2024, **36**, 2311411.
12 H. Peng, B. Cai, Y. Zhang, L. Gao, P. Zhao, L. Zhou, S. Zhang, W. Liang, Q. Xuan, M. Koo, C. Liang, W. Li, Z. Hou, T. Zhou and G. Wang, *Angew. Chem., Int. Ed.*, 2025, **64**, e202421090.
13 A. Levitt, J. Zhang, G. Dion, Y. Gogotsi and J. M. Razal, *Adv. Funct. Mater.*, 2020, **30**, 2000739.
14 C. Wei, Q. Zhang, Z. Wang, W. Yang, H. Lu, Z. Huang, W. Yang and J. Zhu, *Adv. Funct. Mater.*, 2023, **33**, 2211889.
15 X. Zeng, X. Jiang, Y. Ning, F. Y. Hu and B. Fan, *J. Adv. Ceram.*, 2023, **12**, 1562–1576.
16 L. Yao, L. Pan, S. Zhou, H. Liu, H. Mei, Y. Li, K. G. Dassios, P. Colombo, L. Cheng and L. Zhang, *Mater. Horiz.*, 2023, **10**, 3404–3415.
17 Y. Li, Y. Qing, Y. Zhang and H. Xu, *J. Adv. Ceram.*, 2023, **12**, 1946–1960.
18 B. Guo, Y. Wang, C. Cao, Z. Qu, J. Song, S. Li, J. Gao, P. Song, G. Zhang, Y. Shi and L. Tang, *Adv. Sci.*, 2024, **11**, 2309392.
19 Z. Ma, R. Jiang, J. Jing, S. Kang, L. Ma, K. Zhang, J. Li, Y. Zhang, J. Qin, S. Yun and G. Zhang, *Nano-Micro Lett.*, 2024, **16**, 223.
20 J. Hu, Y. Hu, Y. Ye and R. Shen, *Chem. Eng. J.*, 2023, **452**, 139147.
21 V. G. Parale, T. Kim, H. Choi, V. D. Phadtare, R. P. Dhavale, K. Kanamori and H. H. Park, *Adv. Mater.*, 2024, **36**, 2307772.
22 X. Jiang, Q. Wang, L. Song, H. Lu, H. Xu, G. Shao, H. Wang, R. Zhang, C. Wang and B. Fan, *Carbon Energy*, 2024, **6**, e502.
23 Y. Cui, S. Xue, T. Wang, S. Liu, Q. Ye, F. Zhou and W. Liu, *Friction*, 2024, **12**, 1728–1740.
24 Y. Zhan, B. Nan, Y. Liu, E. Jiao, J. Shi, M. Lu and K. Wu, *Chem. Eng. J.*, 2021, **421**, 129733.
25 R. Guo, Y. Fan, L. Wang and W. Jiang, *Carbon*, 2020, **169**, 214–224.
26 G. Mu, D. Mu, B. Wu, C. Ma, J. Bi, L. Zhang, H. Yang and F. Wu, *Small*, 2020, **16**, 1905430.
27 P. Hu, J. Wang, P. Zhang, F. Wu, Y. Cheng, J. Wang and Z. Sun, *Adv. Mater.*, 2023, **35**, 2207638.
28 J. Xu, J. Fang, P. Zuo, Y. Wang and Q. Zhuang, *Adv. Funct. Mater.*, 2024, **34**, 2400732.
29 M. Xu, K. Zhang, L. Wang and Q. Wang, *Composites, Part B*, 2023, **255**, 110616.
30 T. Wang, H. Wang, G. Tan, L. Wang and L. Qiao, *IEEE Trans. Magn.*, 2015, **51**, 1–5.
31 T. Wang, C. Pan, Y. Wang, G. Tan, H. Wang, R. Li and F. Li, *J. Magn. Magn. Mater.*, 2014, **354**, 12–16.
32 C. Liu, T. He, C. Hu, Q. Qian, Y. Hao, L. Xu, H. Lu and G. Ji, *Adv. Funct. Mater.*, 2025, **35**, 16.
33 G. B. Kauffman, *J. Chem. Educ.*, 1988, **65**, 28–31.
34 F. Wu, P. Hu, F. Hu, Z. Tian, J. Tang, P. Zhang, L. Pan, M. W. Barsoum, L. Cai and Z. Sun, *Nano-Micro Lett.*, 2023, **15**, 194.
35 Y. Huang, G. Chen, X. Wang, H. Ma and C. Chai, *J. Mater. Sci.:Mater. Electron.*, 2025, **36**, 33.
36 X. Yin, W. Zheng, H. Tang, L. Yang, C. Lu, L. Pan, P. Zhang and Z. Sun, *Energy Storage Mater.*, 2024, **72**, 103688.
37 X. Wang, Y. Yuan, X. Sun, R. Qiang, Y. Xu, Y. Ma, E. Zhang and Y. Li, *Small*, 2024, **20**, 2311657.
38 Z. Ma, S. Kang, J. Ma, L. Shao, Y. Zhang, C. Liu, A. Wei, X. Xiang, L. Wei and J. Gu, *ACS Nano*, 2020, **14**, 8368–8382.
39 B. Yang, L. Wang, J. Zhao, R. Pang, B. Yuan, J. J. Tan, S. Song, J. Y. Nie and M. Zhang, *ACS Appl. Mater. Interfaces*, 2022, **14**, 47075–47088.
40 L. Wang, M. Zhang, B. Yang and J. Tan, *ACS Appl. Mater. Interfaces*, 2021, **13**, 41933–41945.

41 M. Kruk and M. Jaroniec, *Chem. Mat.*, 2001, **13**, 3169–3183.
42 H. Niu, X. Tu, S. Zhang, Y. Li, H. Wang, G. Shao, R. Zhang, H. Li, B. Zhao and B. Fan, *Chem. Eng. J.*, 2022, **446**, 137260.
43 J. Wang, X. Ma, J. Zhou, F. Du and C. Teng, *ACS Nano*, 2022, **16**, 6700–6711.
44 Y. Du, J. Xu, J. Fang, Y. Zhang, X. Liu, P. Zuo and Q. Zhuang, *J. Mater. Chem. A*, 2022, **10**, 6690–6700.
45 S. Zhao, G. Siqueira, S. Drdova, D. Norris, C. Ubert, A. Bonnin, S. Galmarini, M. Ganobjak, Z. Pan, S. Brunner, G. Nyström, J. Wang, M. M. Koebel and W. J. Malfait, *Nature*, 2020, **584**, 387–392.
46 Z. Yan, Y. Ding, M. Huang, J. Li, Q. Han, M. Yang and W. Li, *ACS Appl. Nano Mater.*, 2023, **6**, 6141–6150.
47 Z. Lu, F. Jia, L. Zhuo, D. Ning, K. Gao and F. Xie, *Composites, Part B*, 2021, **217**, 108853.
48 N. Zhai, J. Luo, P. Shu, J. Mei, X. Li and W. Yan, *Nano Res.*, 2023, **16**, 10698–10706.
49 X. Yang, L. Liang, C. Li, B. Zhang, Y. Zhao, S. Tan and G. Ji, *Nano Lett.*, 2024, **25**, 569–577.
50 M. Zhu, X. Yan, H. Xu, Y. Xu and L. Kong, *Carbon*, 2021, **182**, 806–814.
51 S. Qian, G. Liu, M. Yan and C. Wu, *ACS Appl. Nano Mater.*, 2022, **5**, 9771–9779.
52 J. Liu, H. Zhang, X. Xie, R. Yang, Z. Liu, Y. Liu and Z. Yu, *Small*, 2018, **14**, 1802479.
53 F. Yang, J. Yao, L. Jin, W. Huyan, J. Zhou, Z. Yao, P. Liu and X. Tao, *Composites, Part B*, 2022, **243**, 110161.
54 W. Zhang, E. Ding, W. Zhang, J. Q. Li, C. Luo and L. Zhang, *J. Mater. Chem. C*, 2023, **11**, 9438–9448.
55 W. Pan, M. He, X. Bu, Y. Zhou, B. Ding, T. Huang, S. Huang and S. Li, *J. Mater. Sci.: Mater. Electron.*, 2017, **28**, 8601–8610.
56 J. Zou, Q. Li, E. Zhao, J. Zhang, Y. Wang and J. Yang, *Ceram. Int.*, 2024, **50**, 27530–27539.
57 F. Hu, P. Ding, F. Wu, P. Zhang, W. Zheng, W. Sun, R. Zhang, L. Cai, B. Fan and Z. Sun, *Carbon Energy*, 2024, **6**, e638.
58 F. Hu, H. Tang, F. Wu, P. Ding, P. Zhang, W. Sun, L. Cai, B. Fan, R. Zhang and Z. Sun, *Small Methods*, 2024, **8**, 2301476.
59 S. Zhang, X. Liu, C. Jia, Z. Sun, H. Jiang, Z. Jia and G. Wu, *Nano-Micro Lett.*, 2023, **15**, 204.
60 S. Xu, Z. Jia, D. Lan, Z. Gao, S. Zhang and G. Wu, *Adv. Funct. Mater.*, 2025, 2500304, DOI: **10.1002/adfm.202500304,**.
61 X. Zeng, X. Jiang, Y. Ning, Y. Gao and R. Che, *Nano-Micro Lett.*, 2024, **16**, 213.
62 F. Hu, P. Zhang, F. Wu, Z. Tian, H. Tang, B. Fan, R. Zhang, W. Sun, L. Cai and Z. Sun, *J. Materiomics*, 2024, **10**, 531–542.
63 M. Han, X. Yin, K. Hantanasirisakul, X. Li, A. Iqbal, C. Hatter, B. Anasori, C. M. Koo, T. Torita, Y. Soda, L. Zhang, L. Cheng and Y. Gogotsi, *Adv. Opt. Mater.*, 2019, **7**, 1900267.
64 Y. Guo, Y. Duan, X. Liu, H. Zhang, T. Yuan, N. Wen, C. Li, H. Pan, Z. Fan and L. Pan, *Small*, 2024, **20**, 2308809.
65 T. Liu, L. Li, P. Gao, L. Li and M. Cao, *Mater. Sci. Eng., R*, 2025, **164**, 100982.
66 J. Li, X. Hu, Y. Pan, J. Qian, Z. Qiang, Z. Meng, C. Ye and M. Zhu, *Adv. Funct. Mater.*, 2024, **34**, 2410940.
67 T. Xue, S. Yuan, Y. Yang, X. Wan, Y. Yang, X. Mu, L. Zhang, C. Zhang, W. Fan and T. Liu, *Adv. Funct. Mater.*, 2025, **35**, 2417734.